

A Free-standing Nanoporous NiCoFeMoMn High Entropy Alloy as An Efficient Electrocatalyst Fast Driving Water Splittling

Hao Liu

Tianjin University

Hongye Qin

Tianjin University

Jianli Kang (✉ jianlikang@tju.edu.cn)

Tianjin University

Liyang Ma

Tianjin University

Guoxin Chen

Ningbo Institute of Industrial Technology

Qin Huang

Guangdong Academy of Sciences

Zhijia Zhang

Tianjin Polytechnic University

Enzuo Liu

Tianjin University

Huanming Lu

Ningbo Institute of Material Technology and Engineering, the Chinese Academy of Sciences

Naiqin Zhao

Tianjin University

Article

Keywords: Hydrogen evolution reaction (HER), water splitting, oxygen evolution reaction (OER)

Posted Date: February 25th, 2021

DOI: <https://doi.org/10.21203/rs.3.rs-236378/v1>

License:   This work is licensed under a Creative Commons Attribution 4.0 International License.

[Read Full License](#)

1 A Free-standing Nanoporous NiCoFeMoMn High Entropy Alloy as
2 An Efficient Electrocatalyst Fast Driving Water Splittling

3 *Hao Liu^{1,2,3}, Hongye Qin¹, Jianli Kang^{1*}, Liying Ma^{1*}, Guoxin Chen^{3*}, Qin Huang⁴,*

4 *Zhijia Zhang², Enzuo Liu¹, Huanming Lu³, Naiqin Zhao¹*

5 ¹School of Materials Science and Engineering, Tianjin University, Tianjin 300350,
6 China

7 ²School of Materials Science and Engineering, Tiangong University, Tianjin 300387,
8 China

9 ³Ningbo Institute of Materials Technology & Engineering, Chinese Academy of
10 Sciences, Ningbo 315201, China.

11 ⁴Guangdong Institute of Semiconductor Industrial Technology, Guangdong Academy
12 of Sciences, Guangzhou 510651, China

13 *Corresponding author. E-mail: jianlikang@tju.edu.cn (J. Kang); lyima@tju.edu.cn
14 (L.-Y. Ma); gxchen@nimte.ac.cn (G. Chen)

15 **Abstract**

16 The development of low-cost non-noble metal-based electrocatalysts that can
17 work stably at high current densities for the application of Hydrogen evolution
18 reaction (HER) and oxygen evolution reaction (OER) in electrolyzed water is
19 paramount crucial. Herein, we report a free-standing nanoporous high entropy
20 alloy foil as dual-functional electrocatalyst via a combination of one-step
21 dealloying and polarization, which exhibits excellent electrocatalytic activity in
22 alkaline electrolyte with an extremely small overpotential of 150 mV at 1000

1 mA cm⁻² for HER and a low Tafel slope of 29 mV dec⁻¹ in 1 M KOH solution;
2 At the same current density, the overpotential of OER is only 350 mV. The
3 alkaline electrolyzer using it as both anode and cathode only need a cell voltage
4 of 1.47 V to output a stable current density of 10 mA cm⁻², enabling it as an
5 efficient bifunctional electrocatalyst for alkaline overall water splitting, and
6 remarkably better stability for more than 375 hours of continuous hydrogen
7 production while providing substantial material cost savings relative to platinum.
8 DFT calculations indicate that the ultrahigh HER activity of catalyst is originated
9 from the synergetic effect of optimized hydrogen adsorption in the segregation area
10 and enhanced H₂O adsorption in the un-segregation area produced by spinodal
11 decomposition.

12

13 **Introduction**

14 As a kind of clean energy, hydrogen energy has a huge demand in all over the
15 world, and the annual demand is about 70 million tons. However, the main raw
16 materials for its production are traditional fossil fuels such as natural gas and
17 coal, which not only consume a lot of non-renewable resources, but also bring
18 serious carbon emissions^{1, 2, 3}. Electrolyzed water is an environmentally friendly
19 method for hydrogen production, which is regarded as the best choice for
20 hydrogen production in the future^{4, 5, 6}. However, due to the lack of low-cost
21 electrocatalysts with low overpotential at high current density and still good
22 durability, the practical application of electrolyzed water has been greatly

1 limited^{7, 8, 9}.

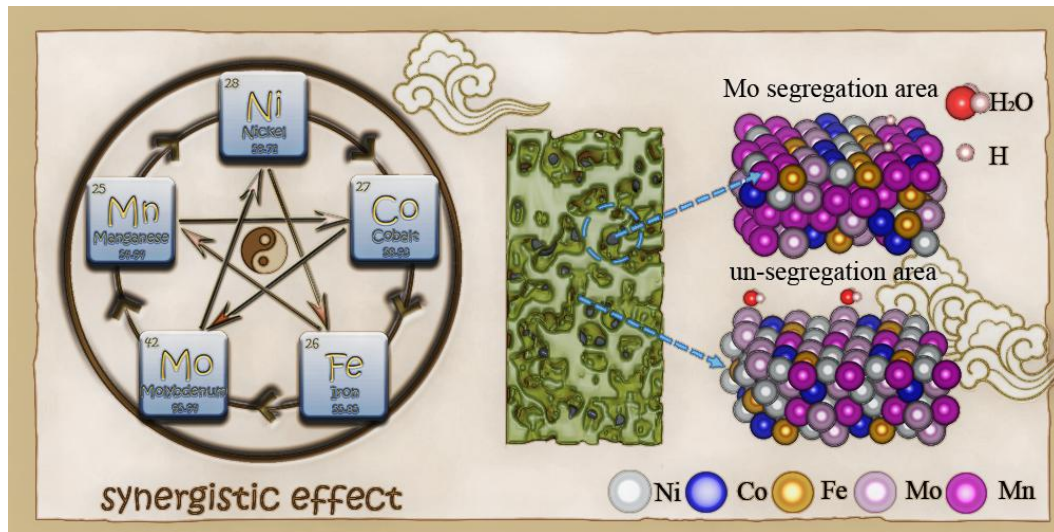
2 Electrolyzed water consists of hydrogen evolution reaction (HER) and
3 oxygen evolution reaction (OER). The reaction kinetics of HER/OER are
4 determined by the binding energy between the active site with reaction
5 intermediate and the water dissociation barrier^{10, 11}. According to the volcanic
6 curve, Pt has the optimized H binding energy and thus has been regarded as the
7 best choice for electrolyzing water. However, the scarcity and high cost of Pt
8 seriously limit its application in electrolytic water^{12, 13}. Therefore, many
9 low-cost transition metal based catalysts have been developed¹⁴, such as
10 transition metal based multicomponent alloys^{15, 16}, carbides¹⁷, phosphide^{14, 18},
11 nitride¹⁹ and sulfides²⁰, or utilizes synergistic effect by stacking the two
12 materials together to construct heterojunction structure to improve the catalytic
13 activity²¹. However, the stable working lifetimes of these catalysts are generally
14 short^{22, 23, 24}. The nanoporous structure of multicomponent alloy is more stable
15 than others material, which is promising to be used as a candidate material for
16 long-term stable work under high current density^{15, 16}.

17 As a new kind of material with unusual microstructure, high entropy alloy
18 (HEA) has mechanical and chemical properties which are incomparable with
19 traditional materials, and has gradually attracted the interest of research in
20 various fields, especially in electrocatalysis^{4, 25, 26}. For example, bulk
21 $\text{Ni}_{20}\text{Fe}_{20}\text{Mo}_{10}\text{Co}_{35}\text{Cr}_{15}$ and $\text{Pt}_{18}\text{Ni}_{26}\text{Fe}_{15}\text{Co}_{14}\text{Cu}_{27}/\text{C}$ show high activities for
22 hydrogen evolution reaction, but their cycle life is only a few hours^{27, 28}.

1 Consequently, it is very important to improve the intrinsic catalytic activity and cycle
2 life of high entropy alloy catalyst for its practical application. HEAs containing two
3 solid solution phases can be formed by spinodal decomposition. Its
4 heterojunction-like structure with controlled electronic structure can be used to
5 improve the intrinsic catalytic activity of the material and inherit the excellent
6 mechanical properties of HEAs to extend work life^{29, 30, 31}.

7 Here, a nanoporous NiCoFeMoMn high entropy alloy (np-HEA), as a
8 bifunctional free-standing catalyst with high HER and OER activities, was
9 prepared by one-step dealloying of Ni₁₄Co₁₄Fe₁₄Mo₆Mn₅₂ multicomponent alloy
10 that produces spinodal decomposition. **Scheme 1** shows the HER process for
11 the nanoporous NiCoFeMoMn HEA. The segregation area by spinodal
12 decomposition is not easy to be dealloyed while the un-segregation area is
13 prone to dealloying, which forms a unique heterojunction structure. Proofed by
14 DFT results, the unique structures of two areas optimize the Gibbs free energies
15 of hydrogen adsorption and H₂O adsorption energy synergistically on active sites,
16 and reduce the dissociation barrier of H₂O so as to enhance the intrinsic
17 catalytic activity of the material. In HER, the current density of 1000 mA cm⁻²
18 can be achieved only with an overpotential of 150 mV in 1 M KOH solution,
19 and the Tafel slope is as low as 29 mV dec⁻¹. OER catalyst was synthesized by
20 polarization of np-HEA, and the overpotential was only 350 mV at the current
21 density of 1000 mA cm⁻². Using them as cathode and anode respectively, the
22 current density of 10 mA cm⁻² can be achieved with only 1.47 V cell voltage,

1 and the excellent stability can be ensured for more than 375 h.



2

3 **Scheme 1.** The HER process for the nanoporous NiCoFeMoMn HEA.

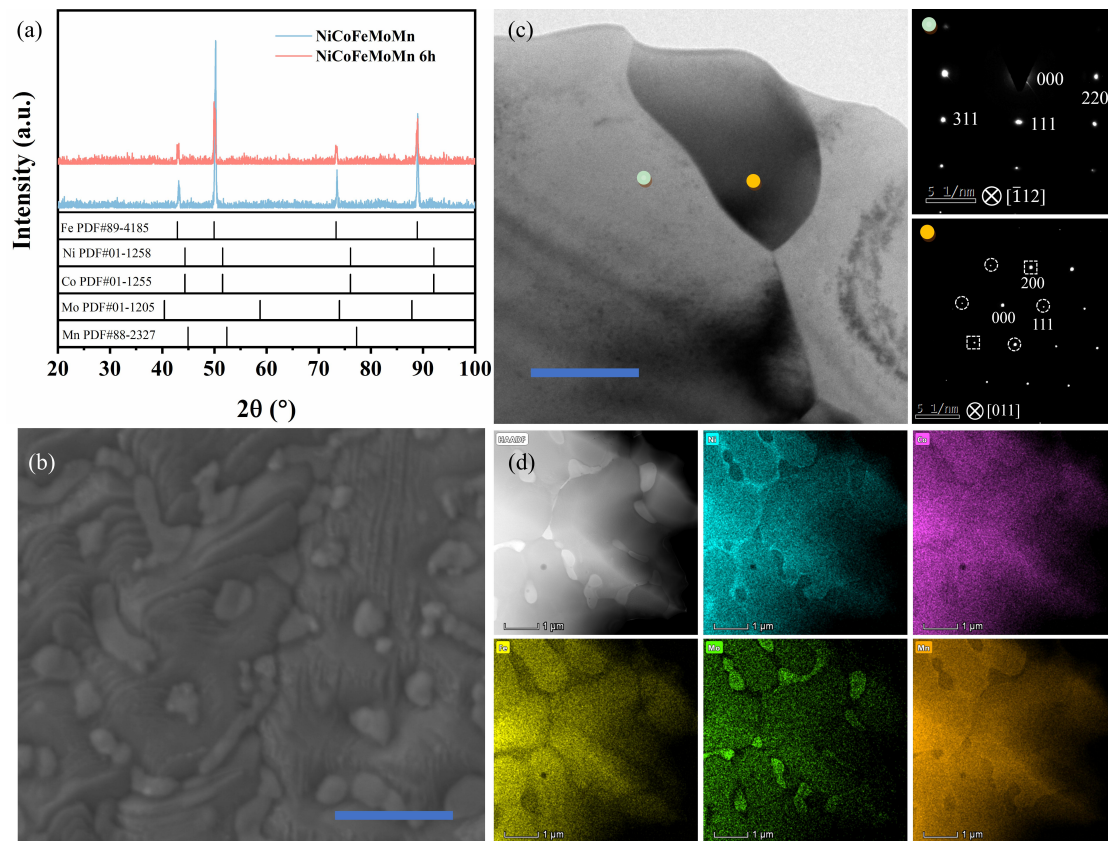
4 **Result**

5 **Material synthesis and characterization.**

6 Firstly, a novel Mn-rich master alloy ($\text{Ni}_{14}\text{Co}_{14}\text{Fe}_{14}\text{Mo}_6\text{Mn}_{52}$) was
7 synthesized by arc melting and single-roller melt spinning. As shown in **Fig. 1a**,
8 X-ray diffraction (XRD) shows four peaks at 43.14, 50.24, 73.51, and 88.98°,
9 which are characteristics of (111), (200), (220) and (311) planes of face
10 centered cubic (FCC) phase. The scanning electron microscopy (SEM) image
11 (**Fig. 1b**) indicates that the spinodal decomposition seems occur due to the
12 appearance of nanoscale (the diameter is 200~300 nm) precipitates at grain
13 boundaries. By Energy-dispersive X-ray spectroscopy (EDS) of SEM proved
14 that the atoms ratio quantified to be Ni, Co, Fe, Mo and Mn is 14.1, 14.4, 14.3,
15 6 and 51.2%, which is consistent with the composition ratio of designed alloys
16 in **Fig. S1** (Supporting Information). In **Fig 1c**, the transmission electron
17 microscopy (TEM) image and the corresponding selected area electron

1 diffraction (SAED) patterns suggested the dual-phase both are FCC phase,
2 confirming that the formation of nanoscale precipitates is due to the spinodal
3 decomposition. The element distribution in the NiCoFeMoMn alloys was
4 characterized by high-angle annual-dark-field scanning TEM (HAADF-STEM)
5 and EDS in **Fig. 1d**. It revealed that the element contents are same as that in
6 SEM-EDS(**Table S1**, Supporting Information). In addition, according to the
7 EDS image, segregation of Mo atoms was found in the NiCoFeMoMn HEA, the
8 composition change will also provide more abundant atomic chemical
9 environment and more active sites, which may improve the performance of
10 electrolyzed water⁴. In order to distinguish, the element segregation area is
11 denoted SA and the other areas are denoted un-SA.

12

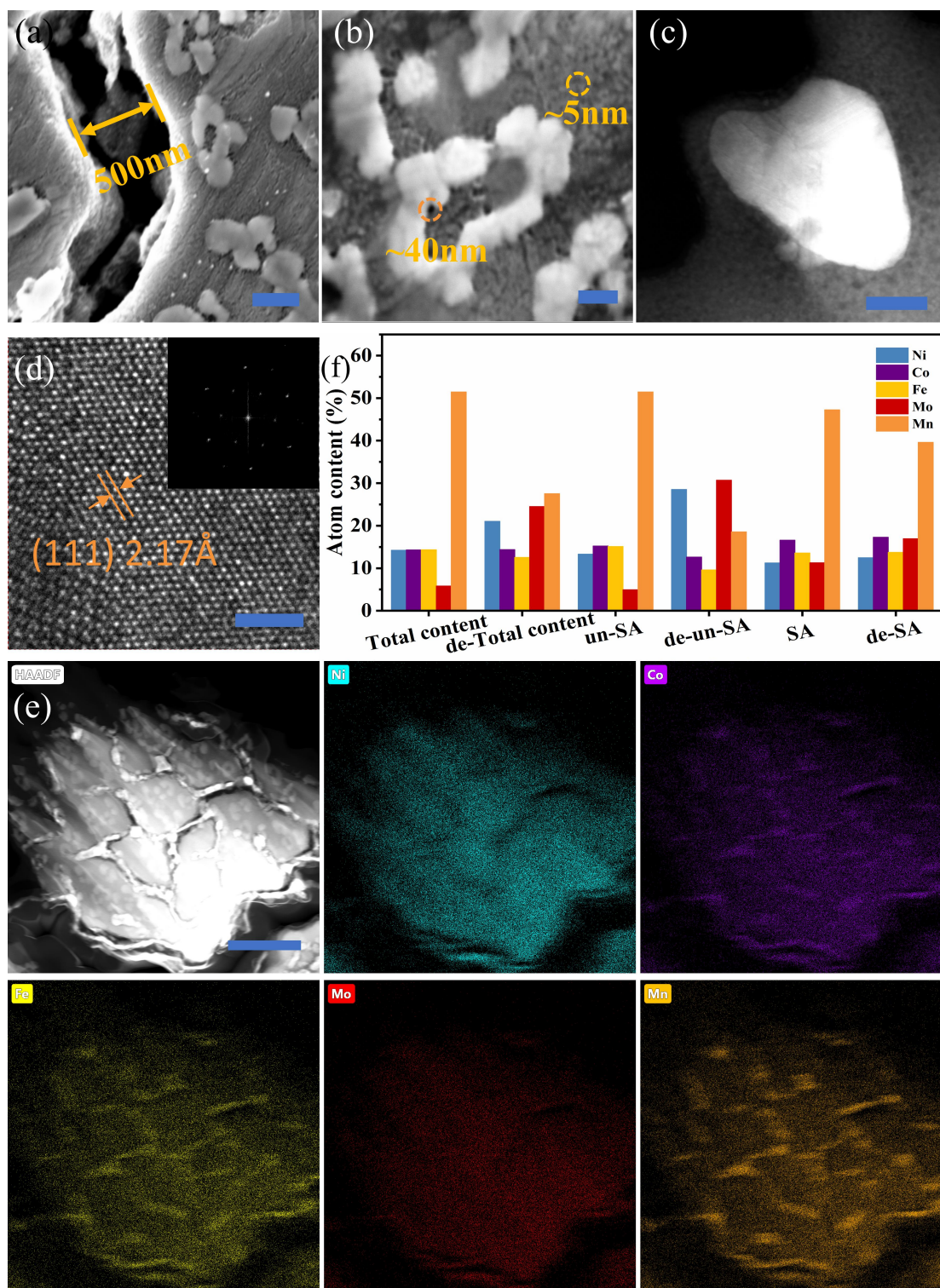


13

1 **Figure 1.** Structural characterization of the master alloy ($\text{Ni}_{14}\text{Co}_{14}\text{Fe}_{14}\text{Mo}_6\text{Mn}_{52}$). (a)
2 XRD analysis of the master alloy and np-NiCoFeMoMn. (b) SEM image of the
3 master alloy. (c) TEM image with corresponding SAED patterns showing. (d)
4 HADDF-STEM image and EDS elemental mapping of the master alloy. Scale bars: b
5 1 μm . c 200 nm. d 1 μm .

6
7 Subsequently, the nanoporous NiCoFeMoMn HEA were prepared by one-step
8 electrochemical dealloying method in 1.0 M $(\text{NH}_4)_2\text{SO}_4$ solution at -0.5 V (vs
9 Ag/AgCl). After dealloying 6 hours, the SEM images in **Fig. 2a** and **2b** show
10 that the cracks with a width of 300~500 nm were formed on the surface of the
11 np-NiCoFeMoMn HEA. In the **Fig. 2b**, it displays a hierarchical nanoporous
12 skeleton with ~5 nm small nanopores on the surface and ~40 nm large
13 nanopores around the SA. N_2 adsorption-desorption measurements further verified
14 that np-NiCoFeMoMn shows a large Brunauer-Emmett-Teller (BET) surface area of
15 45.35 $\text{m}^2 \text{g}^{-1}$ with an average nanopore size of 4.76 nm using the
16 Barrett-Joyner-Halenda (BJH) method (**Fig. S2**). **Fig. 2c** and **Fig. S3** are the
17 HADDF-STEM image of nanoporous NiCoFeMoMn alloy after six hours of
18 dealloying (np-NiCoFeMoMn 6h alloy), which are evidenced the diameter of
19 nanopores around the SA is larger than that of other area. This is due to the
20 potential difference in 1 M $(\text{NH}_4)_2\text{SO}_4$, which is discussed in detail in the
21 Supporting Information. The XRD pattern of np-NiCoFeMoMn ribbons displays
22 a similar crystal structure with the $\text{Ni}_{14}\text{Co}_{14}\text{Fe}_{14}\text{Mo}_6\text{Mn}_{52}$ excepting for a slight

1 shift, inferring that the distance between crystal planes increases with the
2 removal of a part of atoms (in **Fig. 1a** and **Fig. S4**, Supporting Information).
3 This change was also observed by HR-TEM of $\text{Ni}_{14}\text{Co}_{14}\text{Fe}_{14}\text{Mo}_6\text{Mn}_{52}$ in **Fig. S5**
4 and np-NiCoFeMoMn in **Fig. 2d**, the interplanar spacing of (111) planes
5 increased from 2.06 to 2.17 Å after dealloyed. **Fig. 2e** shows the
6 HADDF-STEM-EDS image of np- NiCoFeMoMn 6h, which reveals that Mn, Fe
7 and a small amount of Co are removed after dealloying. Through
8 HADDF-STEM-EDS before and after dealloying, the element atom proportion
9 of each area is summarized in **Fig. 2f**. By comparing the changes of element
10 contents in different regions before and after different dealloying time, it is
11 shown that the dealloying process mainly occurs in un-SA (de-un-SA). The
12 elements composition of Mn, Fe and Co are decreasing, especially the content
13 of Mn decreased from 51.46% to 18.55%. And the composition of SA barely
14 changes when dealloying (de-SA) time is less than six hours (in **Fig. S6**). After
15 that, the SA begins to corrode obviously. Through the quantitative analysis of
16 SEM-EDS, HADDF-STEM-EDS and XPS, it is proved that the surface
17 composition of np-NiCoFeMoMn 6h is consistent (in **Fig. 2e**, **Fig. S7** and **Table**
18 **S1** and **S2**).



1

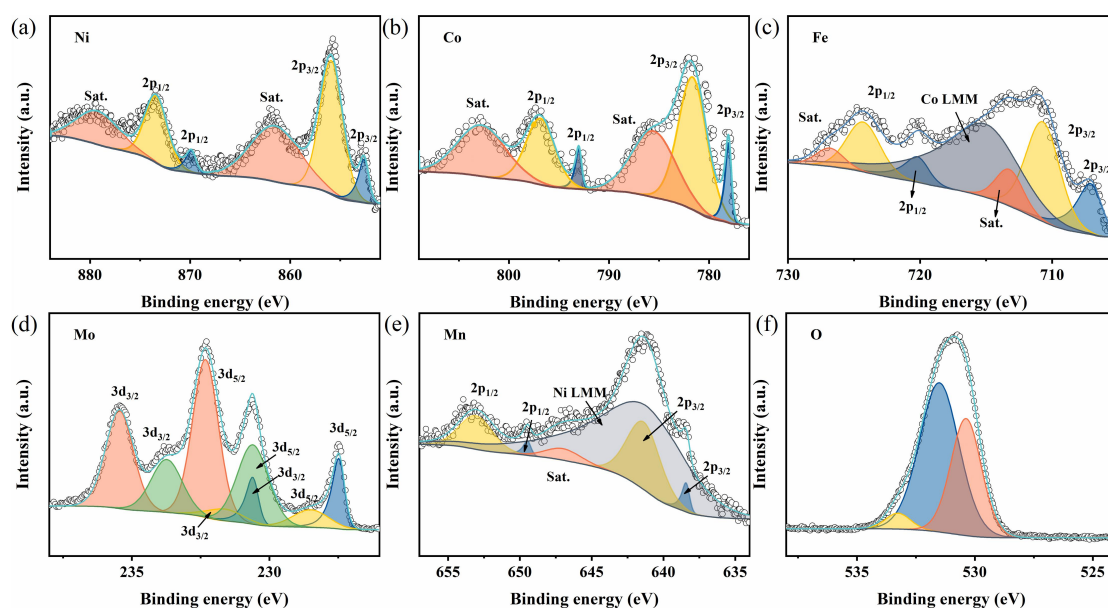
2 **Figure 2.** Structural characterization of np-NiCoFeMoMn. (a) and (b) SEM image of
 3 the np-NiCoFeMoMn. (c) HADDF-STEM of np-NiCoFeMoMn. (d) HR-TEM image
 4 of np-NiCoFeMoMn. (e) HADDF-STEM image and EDS elemental mappings of
 5 np-NiCoFeMoMn. (f) The atomic content of each element in the whole region,

1 including the un-SA and SA of NiCoFeMoMn HEA and np-NiCoFeMoMn HEA.
2 Scale bars: a 300 nm. b 100 nm. c 200 nm. d 2 nm. f 1 μ m.

3
4 To determine the np-NiCoFeMoMn HEA surface chemical states, we also
5 tested X-ray photoelectron spectrometer (XPS) and analyzed the elements of Ni,
6 Co, Fe, Mo, Mn and O (in **Fig. S8** and **Table S3** in the Supporting Information).
7 **Fig. 3a** shows the deconvolution of the Ni 2p core level spectra, which exhibits
8 three peaks of Ni 2p 1/2 with binding energies of 852.62, 855.90 and 861.49 eV
9 assigned to metallic Ni, Ni(II) and relevant satellite peak, respectively³².
10 Among them, Ni(II) is the main valence state with a peak area of 87.3%. Due to
11 the active nature of transition metals, the metallic composition is much lower
12 than that of other states, which is also obvious in other metal elements. In Co 2p
13 region (**Fig. 3b**), Co(II) is the main valence state, and its peak area is 89.3% at
14 781.64 eV (2p 3/2) and 796.84 eV (2p 1/2); the peaks of metallic Co at 778.06
15 (2p 3/2) and 793.03 eV (2p 1/2); the other two peaks (785.54 and 802.77 eV)
16 are satellite peaks. The Fe 2p spectrum in **Fig. 3c** shows seven peaks, two main
17 peaks at 710.30 and 724.30 eV, which can be ascribed to Fe 2p 3/2 and Fe 2p
18 1/2 of Fe(II), respectively; The two smaller peaks (713.23 and 726.83 eV) next
19 to the two main peaks are satellite peaks; The peaks of metallic Fe at 707.10(Fe
20 2p 3/2) and 720.30 eV(Fe 2p 1/2) ¹¹. The peak-fitting analysis of Mo 3d
21 spectrum (**Fig. 3d**) shows that the peak areas of metallic Mo, Mo(II), Mo(IV)
22 and Mo(VI) are 10.0%, 7.9%, 20.9% and 51.2%, respectively¹⁵. From the Mn 2p

1 spectrum (Fig. 3e), according to the characteristic peak at 646.99 eV, we can
 2 judge that the peak of 641.37 and 653.07 eV can be assigned to Mn 2p 3/2 and
 3 Mn 2p 1/2 of Mn(II); The peaks of metallic Mn at 638.43 and 649.48 eV³³. The
 4 O 1s XPS spectrum in Fig. 3f can be simulated by the combination of three
 5 features at 530.37, 531.51 and 533.26 eV, corresponding to the lattice oxygen
 6 (O²⁻), M-OH group and adsorbed oxygen on surface of nanoporous
 7 NiCoFeMoMn alloy³⁴. It is interesting to find that the main oxygen state is
 8 M-OH groups absorbed on the catalyzer surface, which has been reported that it
 9 is beneficial to the adsorption and desorption of H intermediates to accelerate
 10 HER kinetics¹⁵.

11



12

13 **Figure 3.** XPS spectra of np-NiMnFeMo. (a) Ni 2p. (b) Co 2p. (c) Fe 2p. (d) Mo 3d.
 14 (e) Mn 2p. (f) O 1s.

15 **Electrochemical characterizations.**

16 In order to evaluate the electrochemical performance of np-NiCoFeMoMn HEA, a

1 three electrodes configuration was used to perform all electrochemical related tests in
2 1 M KOH solution. The np-NiCoFeMoMn HEA was applied as the working electrode,
3 graphite rod as the counter electrode and Ag/AgCl as the reference electrode. All
4 linear scan voltammogram (LSV) curves were calibrated with reversible hydrogen
5 electrode and IR compensated. The LSV curves of commercial Pt/C and
6 np-NiCoFeMoMn HEA catalysts are exhibited in **Fig. 4a**, the dealloying time of
7 np-NiCoFeMoMn HEA is 0, 3, 4, 5, 6 and 7 hours, respectively. The results show that
8 the overpotential of NiCoFeMoMn 0h is 322 mV at 10 mA cm⁻² current density. After
9 dealloying for 6 hours, the best HER properties were obtained, the overpotential was
10 only ~14 mV at the current density of 10 mA cm⁻², while, the overpotential of
11 commercial Pt/C electrode is 32 mV at 10 mA cm⁻². The Tafel slope is used as the
12 descriptors of the intrinsic activity in HER, calculated by Tafel formula, $\eta = a + b \log$
13 $|j|$ (Where η is the over potential, j is the current density, a is the Tafel constant, and b
14 is the Tafel slope). The results in **Fig. 4b** show that the Tafel slope of
15 np-NiCoFeMoMn HEA 6h has an ultra-low Tafel slope of 29 mV dec⁻¹ that
16 corresponds to the Volmer-Tafel mechanism and the Tafel step ($2H_{ad} \leftrightarrow H_2 + 2*$, H_{ad} is
17 adsorbed hydrogen, $*$ is active site) is the rate determining step of HER, instead of the
18 common Volmer reaction, which is lower than the commercial Pt/C electrode (33 mV
19 dec⁻¹). This mechanism determines that HER kinetics of np-NiCoFeMoMn HEA 6h is
20 faster, and the current density can reach 500 and 1000 mA cm⁻² with 104 and 150 mV
21 overpotential, respectively. However, the overpotential of commercial Pt/C reaches
22 162 mV at current density of 100 mA cm⁻², which is much higher than that of

1 np-NiCoFeMoMn catalyst. Commercial Pt/C catalyst may have high overpotential
2 due to the addition of Nafion. The electrochemical impedance spectroscopy (EIS) was
3 used to further analyze the reason why HER kinetics was greatly improved. The EIS
4 curves of np-NiCoFeMoMn HEA 6h with different dealloying time and commercial
5 Pt/C electrode are shown in **Fig. S9** (Supporting Information). **Fig. S10** shows the
6 equivalent alternative circuits of the electrodes. The semicircle in the curve represents
7 the charge transfer resistance, and the np-NiCoFeMoMn 6h electrode displays a
8 smallest semicircle that represent a lowest charge transfer resistance (R_{ct} is only 22.86
9 Ohm), which is far lower than NiCoFeMoMn 0h (292.8 Ohm). **Fig. S11** shows the
10 EIS curve of np-NiCoFeMoMn 6h, the R_{ct} value decreases rapidly as the overpotential
11 increases, which represents a rapid HER kinetics⁵.

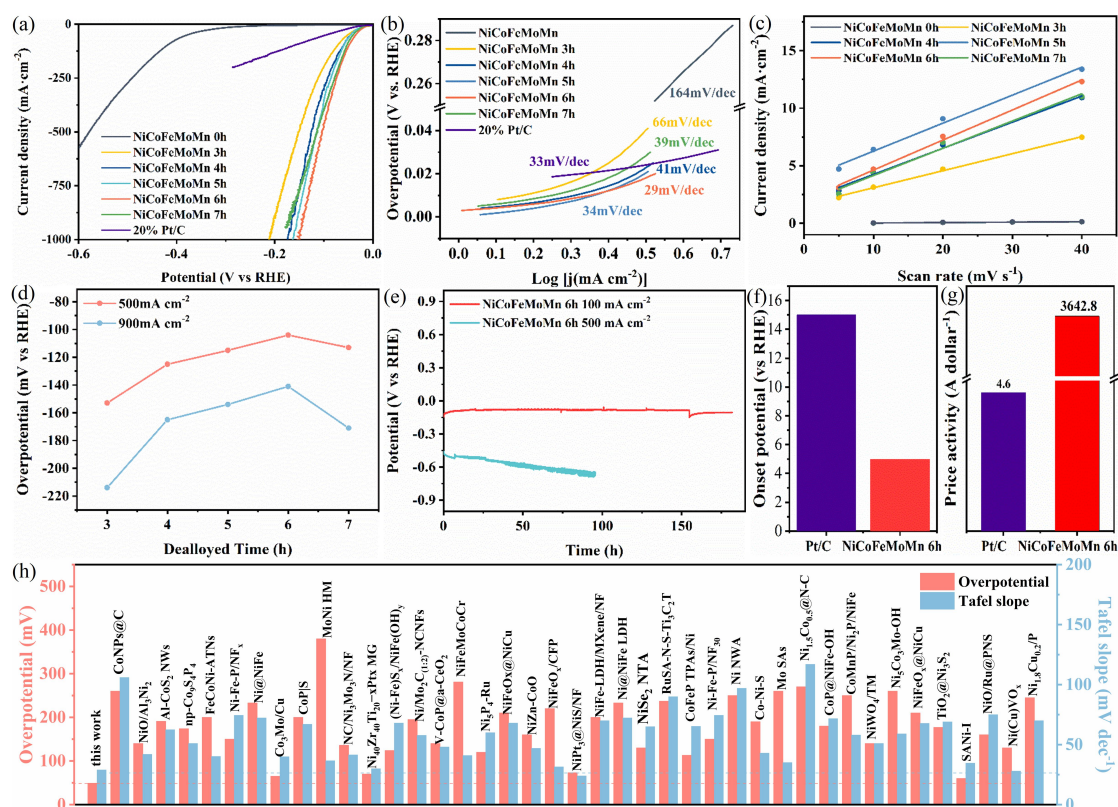
12 The double-layer capacitance (C_{dl}) reflects the electrochemical surface area (ECSA)
13 of the catalyst. In **Fig. S12**, the double-layer capacitance curves of the nanoporous
14 high entropy electrode with different dealloying time are tested by cyclic
15 voltammogram (CV) measurements. The C_{dl} value of the catalyst can be calculated by
16 the curve in **Fig. 4c** and **Fig. S13** with the voltage of 0.15V (vs RHE) at different
17 sweep rates, results reveal a larger C_{dl} of the np-NiCoFeMoMn 6h (261 mF cm⁻²),
18 which is 70 times of NiCoFeMoMn 0h (3.71 mF cm⁻²). As further confirmed by the
19 ECSA results in **Fig. S14** in the Supporting Information, it believes that the
20 hierarchical porous structure and the increased electrochemical active area of the
21 np-NiCoFeMoMn 6h catalyst supply a significant influence on the excellent
22 electrochemical performance. The HER performance of np-NiCoFeMoMn 6h is 160

1 times higher than that of NiCoFeMoMn 0h, which may be due to the formation of
2 larger nanopores near the element SA with the increase of corrosion depth after
3 dealloying, which leads to the exposure of more element segregation area and
4 provides more active sites. In order to confirm this inference, we prepared two
5 ribbons according to the composition of SA and un-SA, respectively. The LSV curves
6 are shown in **Fig. S15**. The results show that the HER performance of the electrodes
7 with SA is higher than un-SA. **Fig. 4d** shows the relationship between the dealloying
8 time and HER performance. The HER performance is improved with increasing
9 dealloying time, the highest of which is obtained when the dealloying time is 6 hours.
10 Then the catalyst performance began to decline with increasing dealloying time as
11 same as that of ECSA, which would be the primary cause for the corresponding
12 declined performance. This infers that the synergistic effect of np-NiCoFeMoMn
13 HEA also appears to have a major contribution to promoted HER performance.

14 As shown in **Fig. 4e**, the np-NiCoFeMoMn can be stably worked in 1 M KOH
15 solution for 180 and 100 h at the current density of 100 and 500 mA cm⁻². After a
16 long-term durability test, the performance of the catalyst did not decline significantly.
17 The SEM images show that the surface structure of catalyst has not changed
18 obviously (**Fig. S16**). Additionally, the np-NiCoFeMoMn 6h electrode shows the
19 onset potential (potential required to reach -1 mA cm⁻²) for HER at 5 mV (**Fig. 4f**),
20 which can only be observed for commercial Pt/C catalyst. Furthermore, by comparing
21 the price activity of np-NiCoFeMoMn 6h electrode and commercial Pt/C electrode at
22 an overpotential of -100 mV (in **Fig. 4g**), the price activity of np-NiCoFeMoMn alloy

1 electrode is as high as 3642 A dollar⁻¹, which is more than 792 times of that of Pt/C
2 electrode, showing that np-NiCoFeMoMn alloy can greatly reduce the cost of HER.
3 This is the mark great advantages for the practical industrial application of
4 nanoporous HEA catalyst. Furthermore, the multi-step chronoamperometric curve in
5 **Fig. S17** and multi-step voltage curve in **Fig. S18** was performed in 1.0 M KOH
6 solution. The multi-step chronoamperometric curve at overpotential starting at 0 mV
7 and ending at 690 mV with an increment of 80 or 300 mV per 2 h. The multi-step
8 voltage curve at current density ranges from 100 to 1400 mA cm⁻². The results reveal
9 that the current remains very stable at each potential in the entire range, which further
10 validates that the material has high catalytic stability in a wide current range (0~1400
11 mA cm⁻²). The low Tafel slope and overpotential of nanoporous HEA are further
12 confirmed by comparison with other catalysts. As shown in **Fig. 4h** and **Table S4**, it is
13 further proved that the catalyst has excellent HER performance. The Tafel slope and
14 the overpotential at 100 mA cm⁻² of 42 kinds of HER catalysts reported recently are
15 compared. The np-NiCoFeMoMn 6h electrode is state-of-the-art non noble metal
16 HER catalyst, and even surpasses the performance of noble metal catalysts.

17

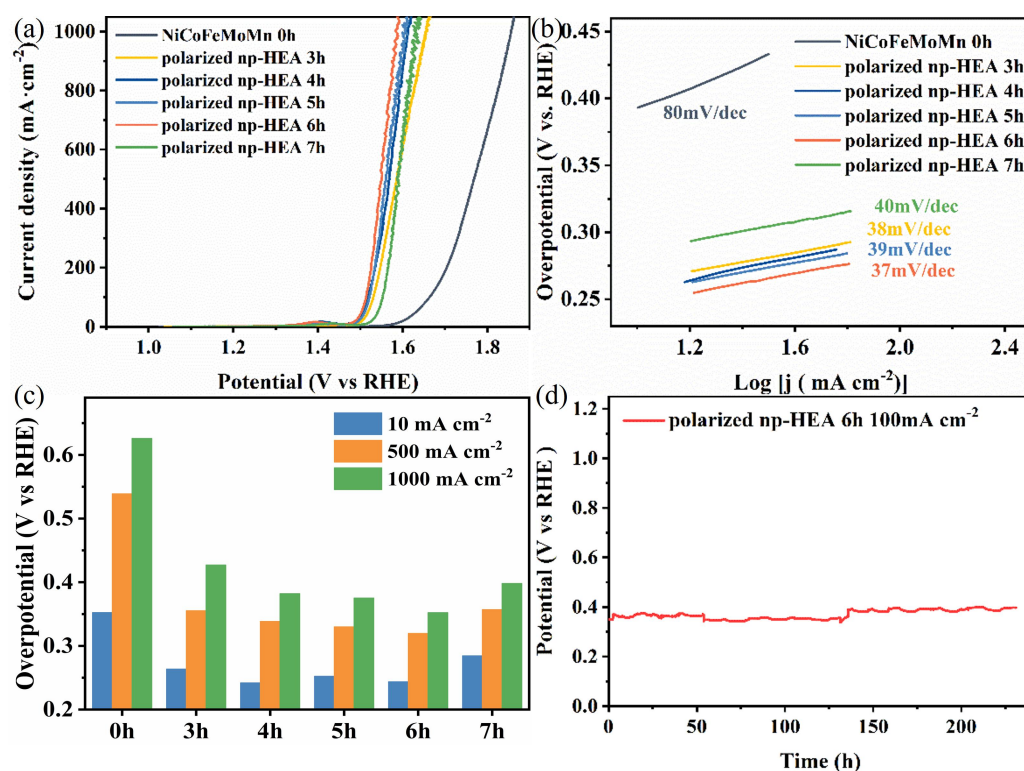


1
 2 **Figure 4.** Electrocatalytic HER performances of the nanoporous catalysts. (a) HER
 3 polarization curves for nanoporous NiCoFeMoMn and commercially available Pt/C in
 4 1 M KOH solution. Scan rate: 1 mV s⁻¹. (b) Tafel plots of different electrocatalytic
 5 materials. (c) The double-layer capacitances (C_{dl}) calculated by the differences in
 6 current densities at 0.15 V (vs RHE) as a linear function of scan rates. (d)
 7 Relationship between dealloying time and HER performance. (e) The time-current
 8 curves of the nanoporous NiCoFeMoMn 6h at a current density of 100 and 500 mA
 9 cm⁻² without iR loss correction. (f) Tafel slope and overpotential at 100 mA cm⁻² of
 10 NiCoFeMoMn 6h electrode, comparing with the values of representative HER
 11 catalysts reported previously.

12
 13 The np-NiCoFeMoMn with perfect corrosion resistance can also be used as the OER

1 catalyst, which is activated by a electrochemical polarization strategy at 1.2 V (vs
2 Ag/AgCl). XPS analysis (**Fig. S19**) indicated that HEA was fully covered by a layer
3 of oxy-hydroxide during polarization. However, the XRD analysis (**Fig. S20**) show no
4 obvious oxide phases form, inferring only a very thin layer of oxy-hydroxide was
5 formed and self-passivated to prevent further oxidation, similar to the previous
6 reports³⁵. **Fig. 5a** and **5b** show the OER performance and the corresponding Tafel
7 slopes of the polarized np-HEA electrode. Obviously, the polarized np-HEA 6h
8 obtained the pick of OER catalysts. The overpotential of polarized np-HEA 6h is 243
9 mV at the current density of 10 mA cm⁻² and the achieved Tafel slope is 37 mV dec⁻¹,
10 respectively. Compared to the Tafel slope of HEA with the value of 80 mV dec⁻¹, the
11 decrease of this value indicates that the polarized np-HEA greatly promoted the four
12 electrons progress in OER, reaction rate of each step was optimized. In **Fig. 5c**, the
13 overpotential of all catalysts at different current densities is compared, which shows
14 that this trend is very close to their HER performance and present a similar volcano
15 shape. In addition to the specific surface area, the OER performance may be affected
16 by the synergistic effect of different dealloying time catalysts. Meanwhile, the
17 excellent OER durability of catalyst comes from its stable structure, it can operate
18 stably for more than 230 h when the current density is 100 mA cm⁻² in 1M KOH
19 solution (**Fig. 5d**), and even at 500 mA cm⁻² it can still work over 100 h (**Fig. S21**).
20 The structure of polarized np-HEA remains in its original state after durability test by
21 SEM (**Fig. S22**), which indicates that polarized np-HEA also has good stability in
22 OER. Due to the formation of oxy-hydroxide on the surface of polarized np-HEA, the

1 material is more stable at high current density. By comparing the OER data with
 2 others literature, the Tafel slope and overpotential at large current density of polarized
 3 np-HEA are very attractive in OER performance in metal-oxide based catalysts and
 4 have great application prospects (Table S5).

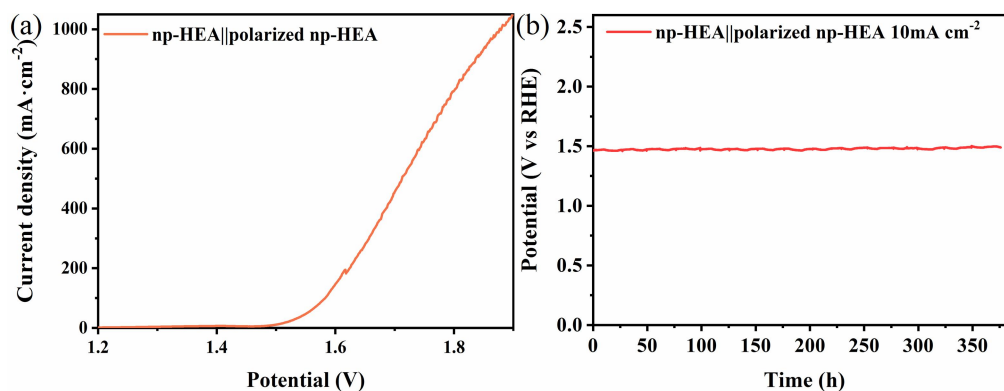


5
 6 **Figure 5.** Electrocatalytic OER performances of the polarized np-HEA catalysts. (a)
 7 OER polarization curves for polarized np-HEA in 1 M KOH solution. Scan rate: 1
 8 mV s^{-1} . (b) Tafel plots of different electrocatalytic materials. (c) Relationship between
 9 dealloying time and OER performance. (d) The time-current curves of the polarized
 10 np-HEA 6h at a current density of 100 mA cm^{-2} without iR.

11 Due to the excellent HER and OER properties of HEA, nanoporous alloy and
 12 polarized np-HEA were used as cathode and anode respectively for full water splitting
 13 test. **Fig. 6a** shows the LSV curve measured in an electrolytic cell with two electrodes
 14 in 1 M KOH solution. It requires a very low cell voltage of 1.47 V to reach 10 mA

1 cm^{-2} . Even at the current density of 500 and 1000 mA cm^{-2} , the cell voltage is 1.7 and
2 1.8 V. This performance is better than many bifunctional catalysts in alkaline
3 electrolytes by compared in **Table S6**. The alkaline electrolyzer using bifunctional
4 electrodes of np-HEA|| polarized np-HEA shows excellent durability for practical use.
5 It can steadily work for continuously full water splitting for as long as 375 h at 10 mA cm^{-2}
6 cm^{-2} (**Fig. 6b**). Furthermore, the durability of np-HEA|| polarized np-HEA electrode as
7 a bifunctional catalyst has higher constancy than previously reported in the literature.

8



9

10 **Figure 6.** Electrocatalytic over water splitting performances of the nanoporous alloy
11 catalysts. (a) Polarization curve of water electrolysis using nano porous
12 NiCoFeMoMn 6h as both HER and OER electrocatalysts in a two-electrode
13 configuration. (b) Chronopotentiometric curve of the nano porous NiCoFeMoMn 6h
14 for water splitting at 10 mA cm^{-2} .

15

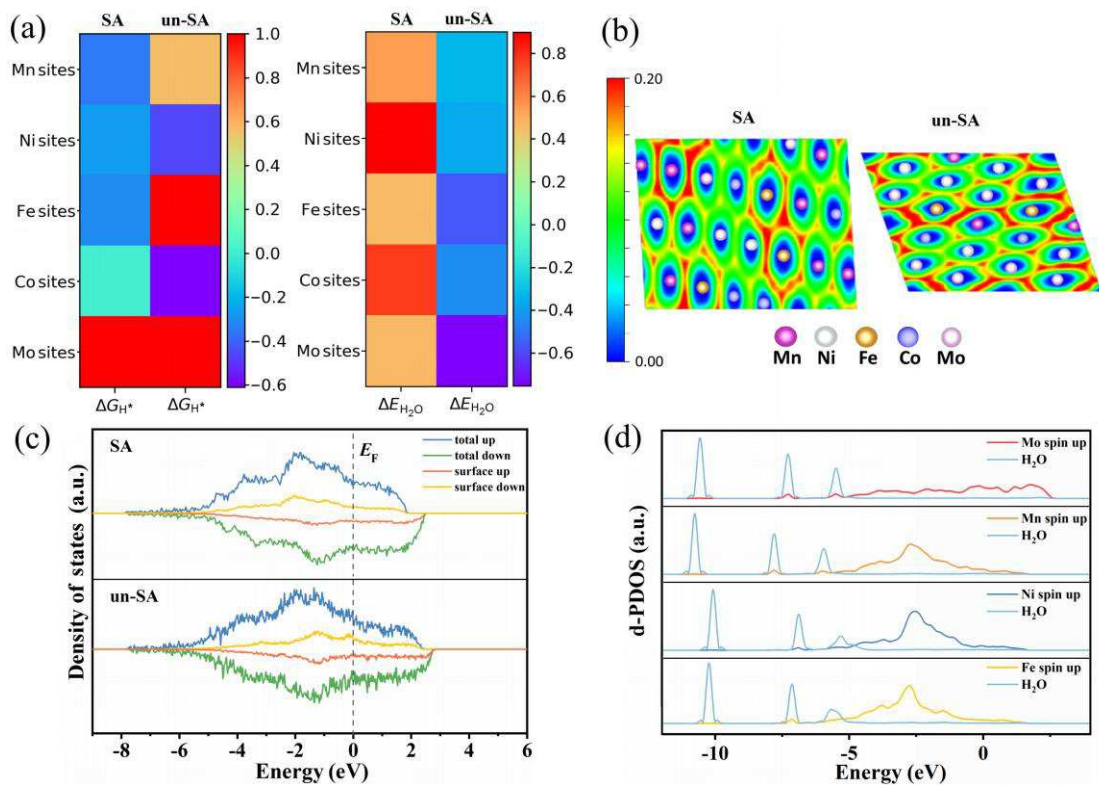
16 Discussion

17 To further understand the HER mechanism, DFT calculations were performed to
18 investigate the modulation essence of catalytic activity. The np-HEA model of SA and

1 un-SA were established, which can be found in Supporting Information. As a
2 well-known descriptor for HER catalysis in basic condition, the calculated Gibbs free
3 energies of hydrogen adsorption (ΔG_{H^*}) of all possible active sites on (111) surface
4 were comprehensively evaluated in **Fig. S23** (SA) and **S24** (un-SA) respectively, seen
5 in Supporting Information. Remarkably, the ΔG_{H^*} value of SA is much closer to the
6 thermo neutral position than that of un-SA. On some active sites of SA in **Fig. S23**,
7 the ΔG_{H^*} on 7, 8 and 16 sites (-0.05, -0.03 and 0.01 eV) exhibit platinum-like catalytic
8 properties (-0.09 eV). In comparison, the enhanced ΔG_{H^*} of un-SA in **Fig. S24** will
9 sluggish the kinetic process of hydrogen production. The colored ΔG_{H^*} comparison of
10 SA and un-SA is presented in **Fig. 7a**. Therefore, the SA in np-HEA plays a crucial
11 role in the hydrogen adsorption characters, which is in good agreement with the
12 experimental results. Moreover, the reasons of proton being most likely to be
13 adsorbed on the hollow position and ΔG_{H^*} of SA being thermo neutral were further
14 explained by the electronic structure analysis including the electron localization
15 functions (ELF) map in **Fig. 7b** and charge density difference in **Fig. S25** of (111)
16 surface on SA and un-SA³⁶. It demonstrates the metal bonding in the compound and
17 the valance electrons in d orbital localizing strongly in the interstices of the nearest
18 three atoms. Specifically, for the two electrons involved HER process, the valance
19 electron localization will guarantee the proton adsorption. Furthermore, the ΔG_{H^*}
20 difference between SA and un-SA can be explained by the density of states in **Fig. 7c**.
21 In comparison with the electronic structure of un-SA, more surface occupied states of
22 SA are delocalized near the Fermi level, which is associated with the thermal neutral

1 ΔG_{H^*} and faster proton transfer kinetics.

2 In addition to the hydrogen adsorption, the H₂O adsorption effect was further
3 unveiled as well. The optimized atomic structures of SA and un-SA can be found in
4 **Fig. S26** and **S27** respectively. The colored H₂O adsorption energy (ΔE_{H_2O})
5 comparison is presented in **Fig. 7a**, which displays that H₂O is much easier to bind
6 with the metal atom on un-SA than those on SA. Overall, the un-SA of HEA is
7 energetically favorable active surface for H₂O adsorption rather than SA. To reveal
8 the relationship of the H₂O adsorption strength on different adsorption sites, the
9 electronic structures of H₂O on un-SA were simulated, which shows that the occupied
10 orbitals of adsorbed H₂O prone to hybridize with the d orbitals of metal atoms near -5
11 eV in **Fig. 7d**. The strong coupling of d orbitals with O 2p orbitals will prompt to the
12 electrons transfer and the dissociation kinetics of water correspondingly. In particular,
13 the d orbitals of Mo and Mn spin up density of state overlapping with the O 2p orbitals
14 of H₂O give rise to much stronger H₂O adsorption energy than that of Ni and Fe. In
15 summary, the synergistic adsorption modulations of proton on SA and H₂O on un-SA
16 promote the hydrogen production consequently.



1

2 **Figure 7.** (a) The colored ΔG_{H^*} and ΔE_{H_2O} comparisons of SA and un-SA; the pure
 3 red area means this site is not easy to be adsorbed. (b) The ELF map of SA and un-SA;
 4 (c) The total and surface density of state of SA and un-SA. (d) The d-PDOS plots of
 5 H₂O and Mo, Mn, Ni and Fe adsorbed by H₂O directly on un-SA surface.

6 In summary, a high entropy alloy of NiCoFeMoMn with hierarchical porous
 7 structure by one-step dealloying can greatly increase the electrochemical active
 8 area and expose more electrochemical active sites, which has great potential for
 9 excellent electrochemical performance. As a self-supported electrode, the
 10 NiCoFeMoMn 6h has not only excellent catalyst activity for HER, but also high
 11 efficiency for OER in alkaline solution even at large current densities. Full working
 12 electrolyzer using the bifunctional electrodes exhibits excellent stability with 10 mA
 13 cm⁻² at a cell voltage of 1.47 V and can steady work 375 h. Moreover, DFT
 14 calculations showed that the intrinsically outstanding performance of NiCoFeMoMn

1 6h is due to the synergistic effect of alloying elements on surface electron density
2 between SA and un-SA, which lowers the energy barrier for H₂O dissociation on
3 un-SA and provides optimal HBE active sites on SA. This work marks an important
4 step forward in the development of low-cost HEA electrocatalyst-based electrolyzers
5 for overall water splitting with high efficiency and stability.

6

7 **Acknowledgements**

8 This work was sponsored by the National Natural Science Foundation of China
9 (52071232, 51871165, 11704277), the National Natural Science Foundation for
10 Young Scientists of China (51801136; 51701142), the Youth Innovation Promotion
11 Association CAS (2019295), Guangdong Academy of Sciences construction of
12 domestic first-class institutional action special fund project
13 (2020GDASYL-202001031200).

14 **Author contributions**

15 J.L.K. and Y.L.M. and G.X.C conceived and designed the experiments. H.L.
16 performed the preparation of nanoporous high entropy alloy materials, microstructural
17 characterizations, electrochemical measurements and conducted the STEM
18 characterizations and wrote the paper. H.Y.Q. performed the DFT calculations and
19 wrote the paper. N.Q.Z., H.M.L., Q.H., E.Z.L. and Z.J.Z. discussed the results. All the
20 authors contributed to and commented on this paper.

21 **Competing interests**

22 The authors declare no competing interests.

1

2 **References**

- 3 1. You B, Tang MT, Tsai C, Abild-Pedersen F, Zheng X, Li H. Enhancing
4 Electrocatalytic Water Splitting by Strain Engineering. *Adv Mater* **31**, 1807001
5 (2019).
6
- 7 2. Wang M, *et al.* Theoretical Expectation and Experimental Implementation of In
8 Situ Al-Doped CoS₂ Nanowires on Dealloying-Derived Nanoporous Intermetallic
9 Substrate as an Efficient Electrocatalyst for Boosting Hydrogen Production. *ACS*
10 *Catal* **9**, 1489-1502 (2019).
11
- 12 3. Podjaski F, *et al.* Rational strain engineering in delafossite oxides for highly
13 efficient hydrogen evolution catalysis in acidic media. *Nat Catal* **3**, 55-63 (2019).
14
- 15 4. Jia Z, *et al.* A Novel Multinary Intermetallic as an Active Electrocatalyst for
16 Hydrogen Evolution. *Adv Mater* **32**, 2000385 (2020).
17
- 18 5. Wu Q, *et al.* Identifying Electrocatalytic Sites of the Nanoporous
19 Copper–Ruthenium Alloy for Hydrogen Evolution Reaction in Alkaline
20 Electrolyte. *ACS Energy Lett*, 192-199 (2019).
21
- 22 6. Jiang P, *et al.* Tuning the Activity of Carbon for Electrocatalytic Hydrogen
23 Evolution via an Iridium-Cobalt Alloy Core Encapsulated in Nitrogen-Doped
24 Carbon Cages. *Adv Mater* **30**, 1705324 (2018).
25
- 26 7. Yao R-Q, *et al.* Nanoporous Palladium–Silver Surface Alloys as Efficient and
27 pH-Universal Catalysts for the Hydrogen Evolution Reaction. *ACS Energy Lett* **4**,
28 1379-1386 (2019).
29
- 30 8. Jiang K, *et al.* Single platinum atoms embedded in nanoporous cobalt selenide as
31 electrocatalyst for accelerating hydrogen evolution reaction. *Nat Commun* **10**,
32 1743 (2019).
33
- 34 9. Zhang Y, Luo M, Yang Y, Li Y, Guo S. Advanced Multifunctional Electrocatalysts
35 for Energy Conversion. *ACS Energy Lett* **4**, 1672-1680 (2019).
36
- 37 10. Wang X, Zheng Y, Sheng W, Xu ZJ, Jaroniec M, Qiao S-Z. Strategies for design of
38 electrocatalysts for hydrogen evolution under alkaline conditions. *Mater Today* **36**,
39 125-138 (2020).
40
- 41 11. Wang Y, *et al.* Lattice-Strain Engineering of Homogeneous NiS_{0.5} Se_{0.5}
42 Core-Shell Nanostructure as a Highly Efficient and Robust Electrocatalyst for
43 Overall Water Splitting. *Adv Mater* **32**, 2000231 (2020).

- 1
2 12. Xu W, *et al.* A highly efficient electrocatalyst based on amorphous Pd–Cu–S
3 material for hydrogen evolution reaction. *J Mater Chem A* **5**, 18793-18800 (2017).
4
5 13. Dinh C-T, *et al.* Multi-site electrocatalysts for hydrogen evolution in neutral media
6 by destabilization of water molecules. *Nat Energy* **4**, 107-114 (2018).
7
8 14. Hong W, *et al.* Self-supported nanoporous cobalt phosphosulfate electrodes for
9 efficient hydrogen evolution reaction. *Appl Catal B-Environ* **251**, 213-219 (2019).
10
11 15. Shi H, *et al.* Spontaneously separated intermetallic Co₃Mo from nanoporous
12 copper as versatile electrocatalysts for highly efficient water splitting. *Nat*
13 *Commun* **11**, 2940 (2020).
14
15 16. Liu H, *et al.* Free-standing nanoporous NiMnFeMo alloy: An efficient
16 non-precious metal electrocatalyst for water splitting. *Chem Eng J* **404**, 126530
17 (2021).
18
19 17. Li S, Yang J, Song C, Zhu Q, Xiao D, Ma D. Iron Carbides: Control Synthesis and
20 Catalytic Applications in CO_x Hydrogenation and Electrochemical HER. *Adv*
21 *Mater* **31**, 1901796 (2019).
22
23 18. Li G, *et al.* Cobalt-Cobalt Phosphide Nanoparticles@Nitrogen-Phosphorus Doped
24 Carbon/Graphene Derived from Cobalt Ions Adsorbed Saccharomycete Yeasts as
25 an Efficient, Stable, and Large-Current-Density Electrode for Hydrogen Evolution
26 Reactions. *Adv Funct Mater* **28**, 1801332 (2018).
27
28 19. Chen Y, *et al.* Metallic Ni₃Mo₃N Porous Microrods with Abundant Catalytic Sites
29 as Efficient Electrocatalyst for Large Current Density and Superstability of
30 Hydrogen Evolution Reaction and Water Splitting. *Appl Catal B-Environ* **272**,
31 118956 (2020).
32
33 20. Gao MY, *et al.* Scalable one-step electrochemical deposition of nanoporous
34 amorphous S-doped NiFe₂O₄/Ni₃Fe composite films as highly efficient
35 electrocatalysts for oxygen evolution with ultrahigh stability. *J Mater Chem A* **6**,
36 1551-1560 (2018).
37
38 21. Yang G, *et al.* Interfacial Engineering of MoO₂ -FeP Heterojunction for Highly
39 Efficient Hydrogen Evolution Coupled with Biomass Electrooxidation. *Adv Mater*
40 **32**, 2000455 (2020).
41
42 22. Cui Y, *et al.* Tungsten Oxide/Carbide Surface Heterojunction Catalyst with High
43 Hydrogen Evolution Activity. *ACS Energy Lett* **5**, 3560-3568 (2020).
44

- 1 23. Lin Y, *et al.* Construction of CoP/NiCoP Nanotadpoles Heterojunction Interface
2 for Wide pH Hydrogen Evolution Electrocatalysis and Supercapacitor. *Adv Energy*
3 *Mater* **9**, 1901213 (2019).
4
- 5 24. Wang C, Lu H, Mao Z, Yan C, Shen G, Wang X. Bimetal Schottky Heterojunction
6 Boosting Energy - Saving Hydrogen Production from Alkaline Water via Urea
7 Electrocatalysis. *Adv Funct Mater* **30**, 2000556 (2020).
8
- 9 25. Qiu H-J, *et al.* Nanoporous high-entropy alloys for highly stable and efficient
10 catalysts. *J Mater Chem A* **7**, 6499-6506 (2019).
11
- 12 26. Liu M, Zhang Z, Okejiri F, Yang S, Zhou S, Dai S. Entropy-Maximized Synthesis
13 of Multimetallic Nanoparticle Catalysts via a Ultrasonication - Assisted Wet
14 Chemistry Method under Ambient Conditions. *Adv Mater Interfaces* **6**, 19300015
15 (2019).
16
- 17 27. Zhang G, *et al.* High entropy alloy as a highly active and stable electrocatalyst for
18 hydrogen evolution reaction. *Electrochimica Acta* **279**, 19-23 (2018).
19
- 20 28. Li H, *et al.* Fast site-to-site electron transfer of high-entropy alloy nanocatalyst
21 driving redox electrocatalysis. *Nat Commun* **11**, 5437 (2020).
22
- 23 29. Nellaiappan S, *et al.* High-Entropy Alloys as Catalysts for the CO₂ and CO
24 Reduction Reactions: Experimental Realization. *ACS Catal* **10**, 3658-3663 (2020).
25
- 26 30. Pedersen JK, Batchelor TAA, Bagger A, Rossmeisl J. High-Entropy Alloys as
27 Catalysts for the CO₂ and CO Reduction Reactions. *ACS Catal* **10**, 2169-2176
28 (2020).
29
- 30 31. Jin Z, *et al.* Nanoporous Al-Ni-Co-Ir-Mo High-Entropy Alloy for Record-High
31 Water Splitting Activity in Acidic Environments. *Small*, 1904180 (2019).
32
- 33 32. Jiang K, *et al.* Dynamic active-site generation of atomic iridium stabilized on
34 nanoporous metal phosphides for water oxidation. *Nat Commun* **11**, 2701 (2020).
35
- 36 33. Schipper DE, *et al.* A TiO₂/FeMnP Core/Shell Nanorod Array Photoanode for
37 Efficient Photoelectrochemical Oxygen Evolution. *ACS Nano* **11**, 4051-4059
38 (2017).
39
- 40 34. Li M, Zhu Y, Wang H, Wang C, Pinna N, Lu X. Ni Strongly Coupled with Mo₂C
41 Encapsulated in Nitrogen-Doped Carbon Nanofibers as Robust Bifunctional

1 Catalyst for Overall Water Splitting. *Adv Energy Mater* **9**, 1803185 (2019).

2

3 35. Kang J, Hirata A, Chen L, Zhu S, Fujita T, Chen M. Extraordinary Supercapacitor
4 Performance of a Multicomponent and Mixed-Valence Oxyhydroxide. *Angew*
5 *Chem Int Ed Engl* **54**, 8100-8104 (2015).

6

7 36. Savin A, Nesper R, Wengert S, Fessler TF. ELF: The electron localization function.
8 *Angew Chem Int Edit* **36**, 1809-1832 (1997).

9

10

Figures

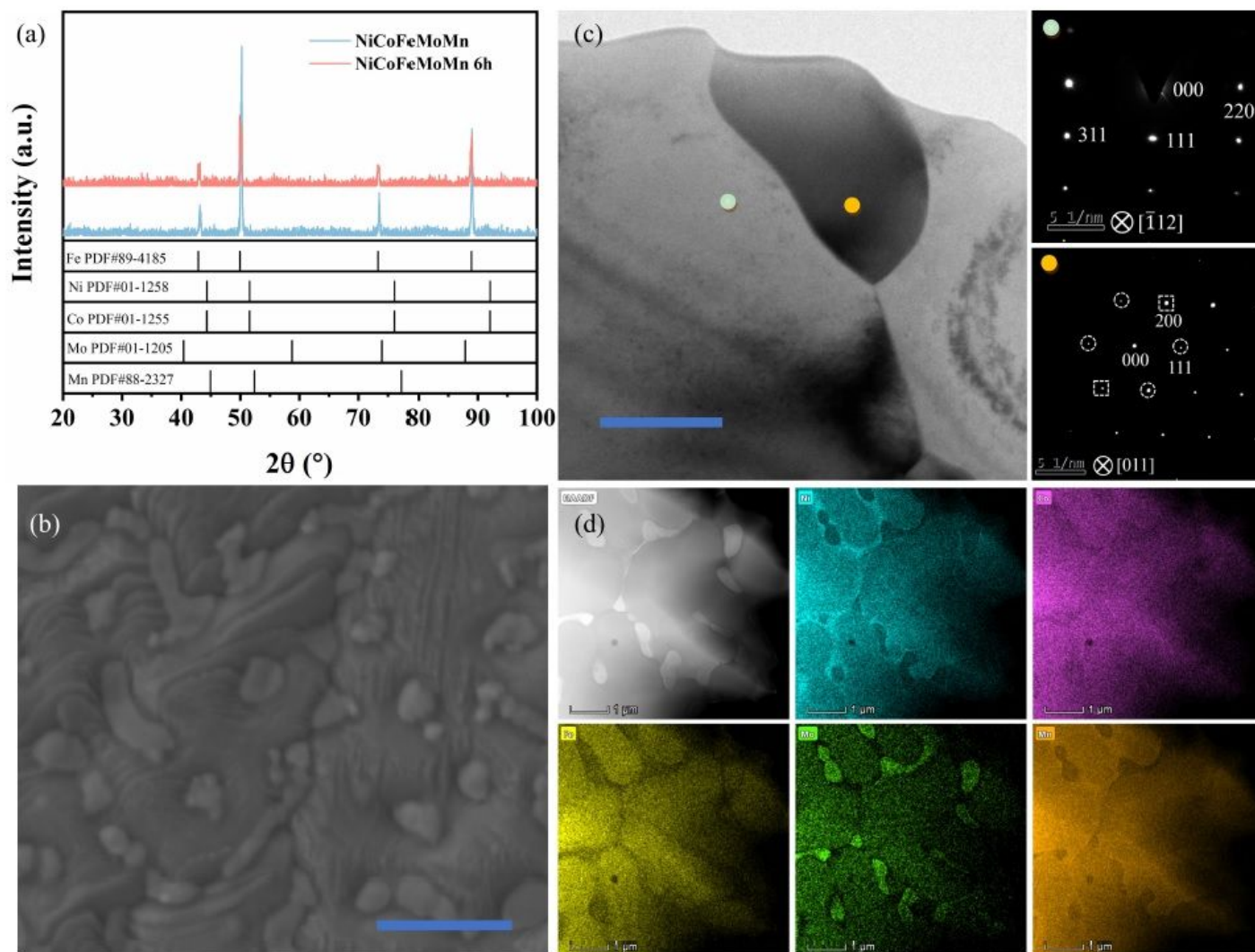


Figure 1

Structural characterization of the master alloy ($\text{Ni}_{14}\text{Co}_{14}\text{Fe}_{14}\text{Mo}_6\text{Mn}_{52}$). (a) XRD analysis of the master alloy and np-NiCoFeMoMn. (b) SEM image of the master alloy. (c) TEM image with corresponding SAED patterns showing. (d) HADDF-STEM image and EDS elemental mapping of the master alloy. Scale bars: b 1 μm . c 200 nm. d 1 μm .

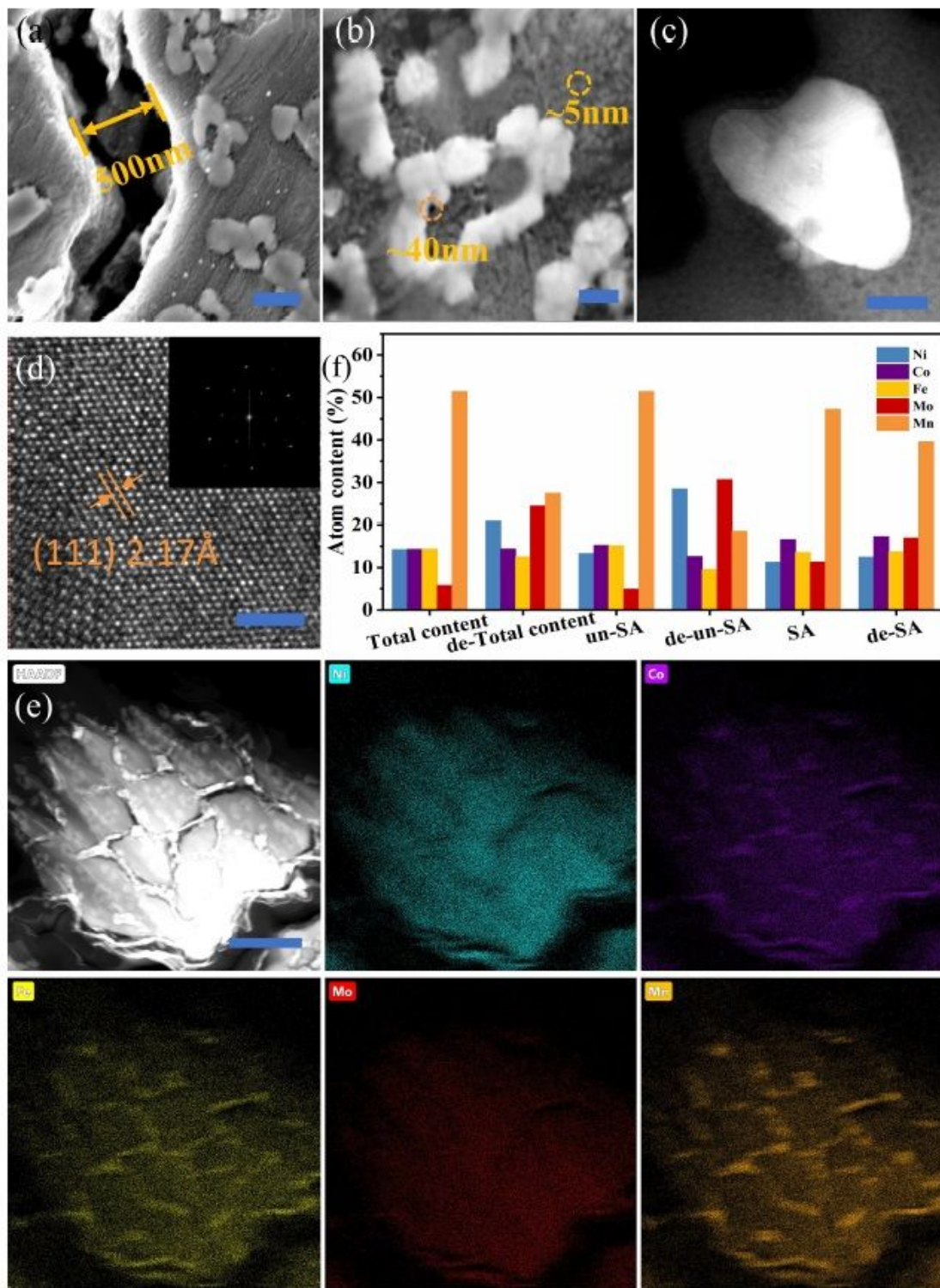


Figure 2

Structural characterization of np-NiCoFeMoMn. (a) and (b) SEM image of the np-NiCoFeMoMn. (c) HADDF-STEM of np-NiCoFeMoMn. (d) HR-TEM image of np-NiCoFeMoMn. (e) HADDF-STEM image and EDS elemental mappings of np-NiCoFeMoMn. (f) The atomic content of each element in the whole region, including the un-SA and SA of NiCoFeMoMn HEA and np-NiCoFeMoMn HEA. Scale bars: a 300 nm. b 100 nm. c 200 nm. d 2 nm. f 1 μ m.

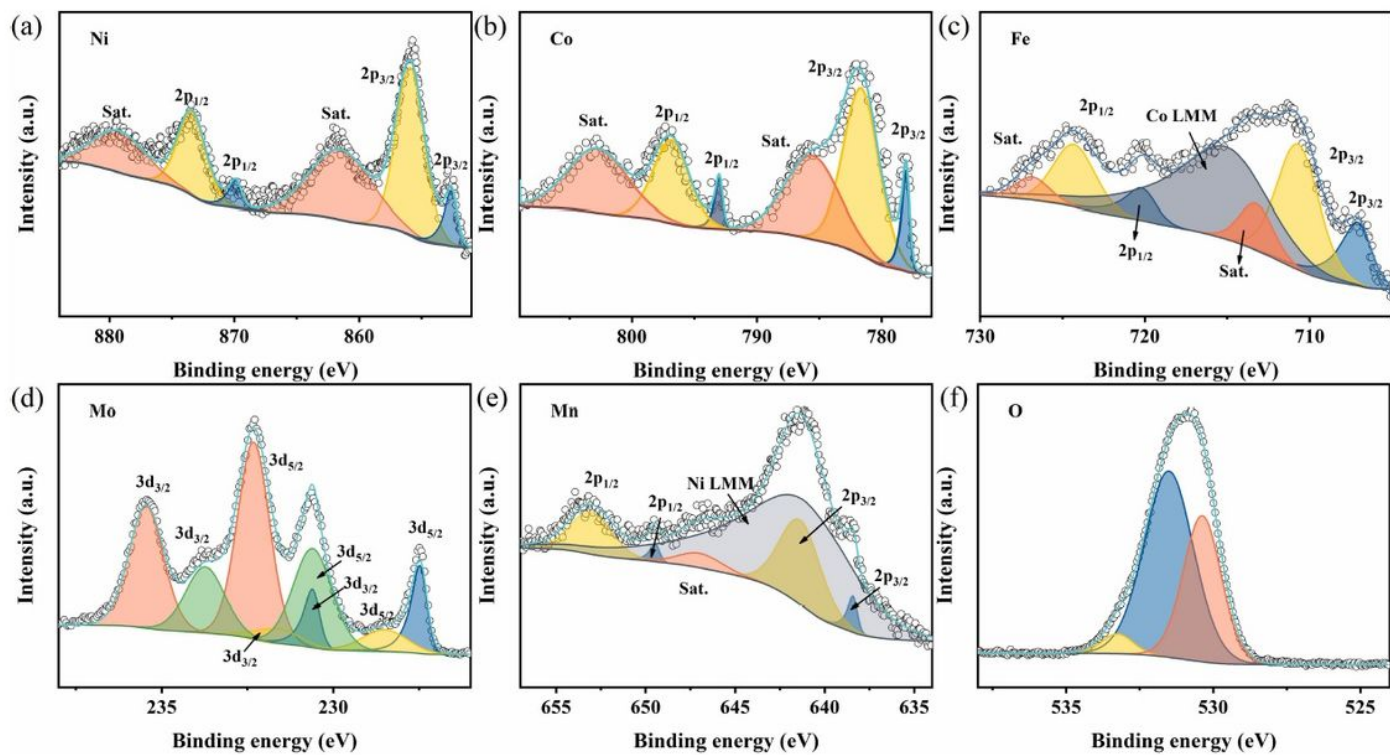


Figure 3

XPS spectra of np-NiMnFeMo. (a) Ni 2p. (b) Co 2p. (c) Fe 2p. (d) Mo 3d. (e) Mn 2p. (f) O 1s.

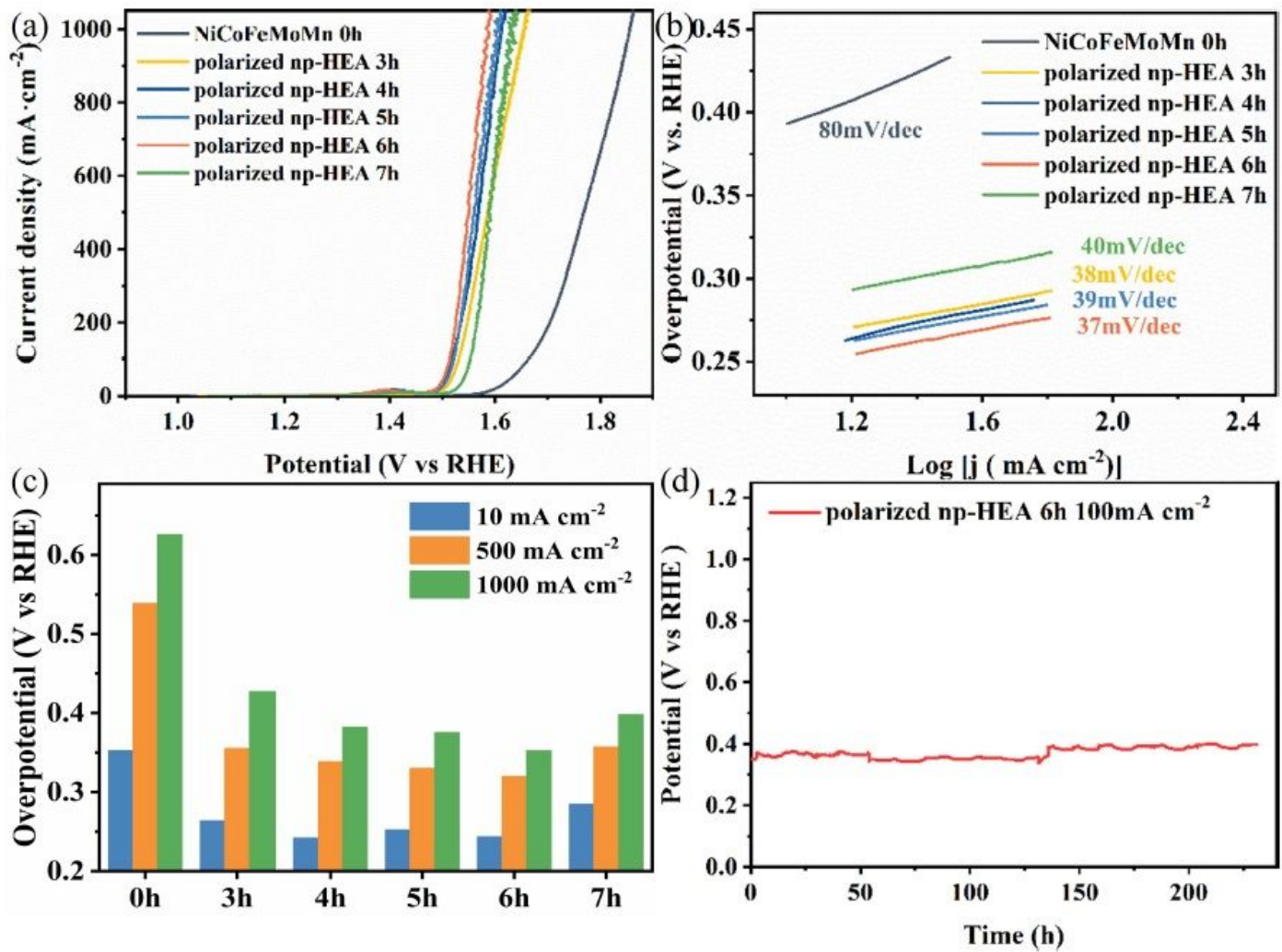


Figure 5

Electrocatalytic OER performances of the polarized np-HEA catalysts. (a) OER polarization curves for polarized np-HEA in 1 M KOH solution. Scan rate: mV s^{-1} . (b) Tafel plots of different electrocatalytic materials. (c) Relationship between dealloying time and OER performance. (d) The time-current curves of the polarized np-HEA 6h at a current density of 100 mA cm^{-2} without iR.

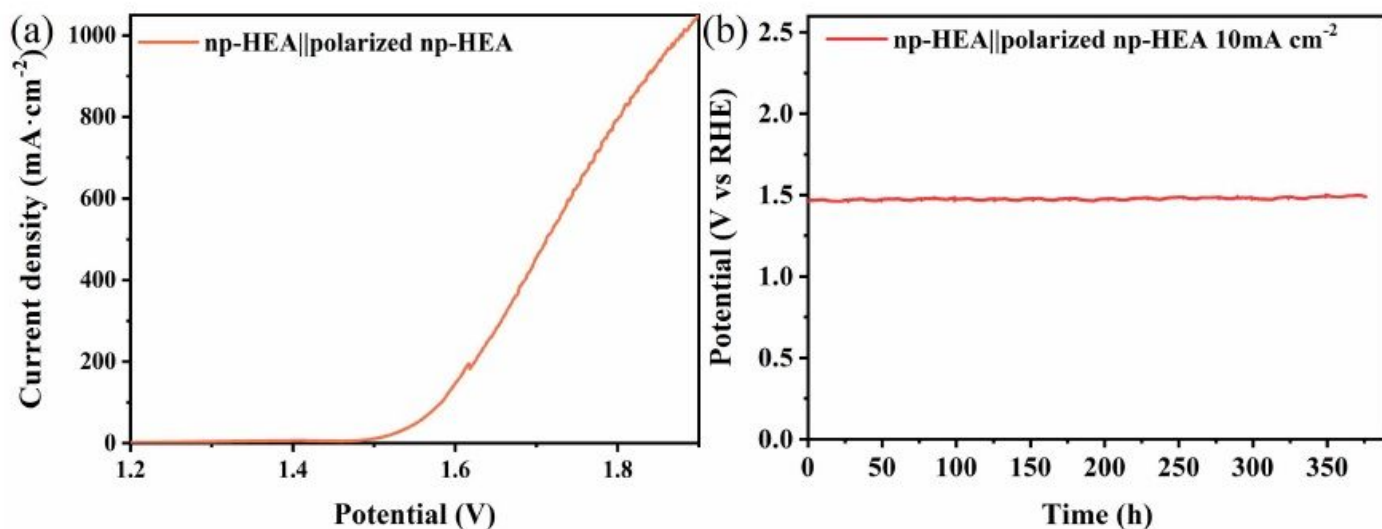


Figure 6

Electrocatalytic over water splitting performances of the nanoporous alloy catalysts. (a) Polarization curve of water electrolysis using nano porous NiCoFeMoMn 6h as both HER and OER electrocatalysts in a two-electrode configuration. (b) Chronopotentiometric curve of the nano porous NiCoFeMoMn 6h for water splitting at 10 mA cm^{-2} .

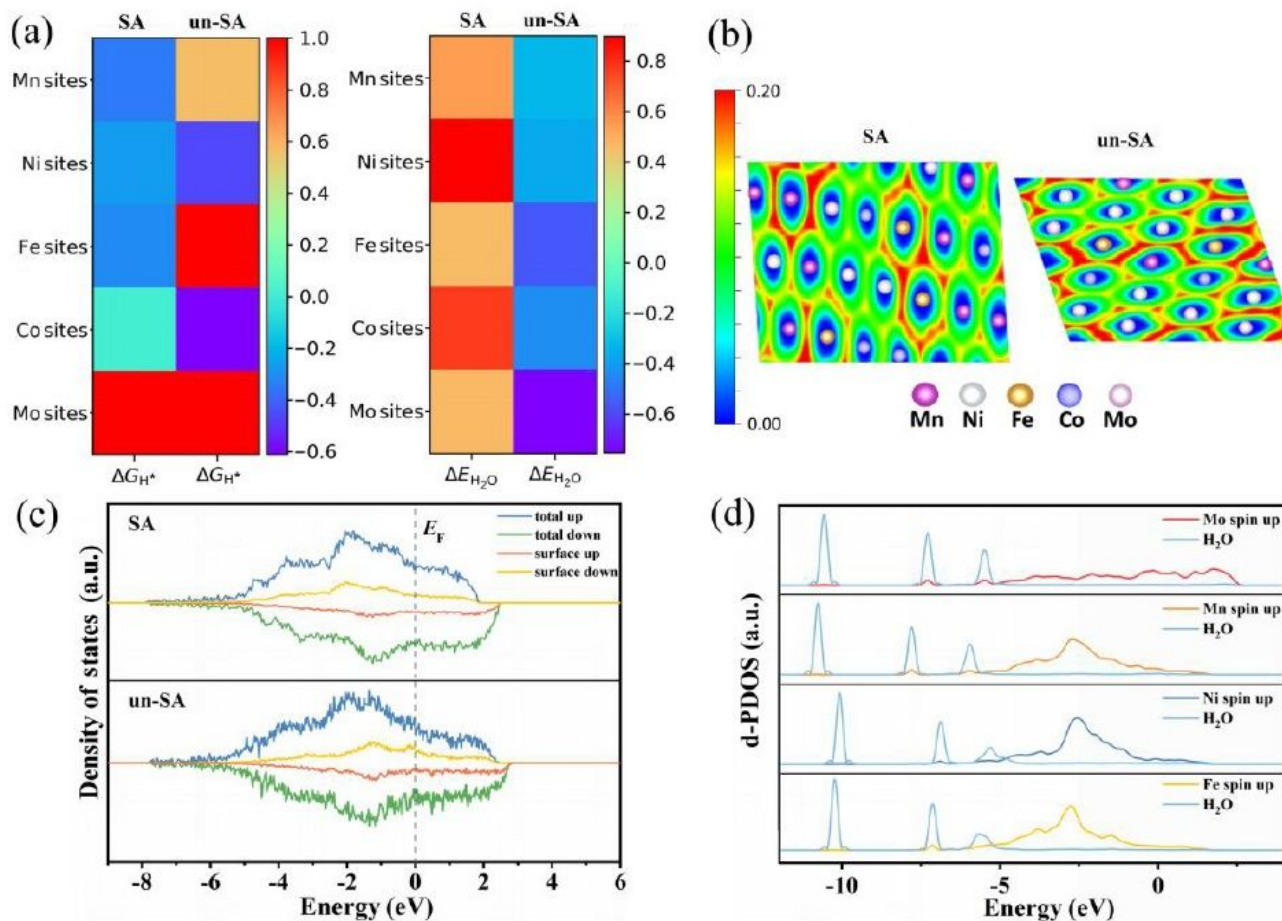


Figure 7

(a) The colored ΔG^* and H₂O 2 E comparisons of SA and un-SA; the pure red area means this site is not easy to be adsorbed. (b) The ELF map of SA and un-SA; (c) The total and surface density of state of SA and un-SA. (d) The d-PDOS plots of H₂O and Mo, Mn, Ni and Fe adsorbed by H₂O directly on un-SA surface.

Supplementary Files

This is a list of supplementary files associated with this preprint. Click to download.

- [SupportingInformation.pdf](#)